Greenlighting Photoelectrochemical Oxidation of Water by Iron Oxide

Dong Wook Kim,[†,‡] Shannon C. Riha,[§] Erica J. DeMarco,[†,‡] Alex B. F. Martinson,[‡,§] Omar K. Farha,[†,∥] and Joseph T. Hupp[*,†,‡,§,⊥]

[†]Department of Chemistry and [‡]Argonne-Northwestern Solar Energy Research (ANSER) Center, Northwestern University, Evanston, Illinois 60208, United States, [§]Materials Science Division, and [⊥]Chemical Sciences and Engineering Division, Argonne National Laboratory, Argonne, Illinois 60439, United States, and [∥]Department of Chemistry, Faculty of Science, King Abdulaziz University, Jeddah 22254, Saudi Arabia

ABSTRACT Hematite (α-Fe_2O_3) is one of just a few candidate electrode materials that possess all of the following photocatalyst-essential properties for scalable application to water oxidation: excellent stability, earth-abundance, suitability positive valence-band-edge energy, and significant visible light absorptivity. Despite these merits, hematite's modest oxygen evolution reaction kinetics and its poor efficiency in delivering photogenerated holes, especially holes generated by green photons, to the electrode/solution interface, render it ineffective as a practical water-splitting catalyst. Here we show that hole delivery and catalytic utilization can be substantially improved through Ti alloying, *provided that the alloyed material is present in ultrathin-thin-film form*. Notably, the effects are most pronounced for charges photogenerated by photons with energy comparable to the band gap for excitation of Fe(3d) → Fe(3d) transitions (*i.e.*, green photons). Additionally, at the optimum Ti substitution level the lifetimes of surface-localized holes, competent for water oxidation, are extended. Together these changes explain an overall improvement in photoelectrochemical performance, especially enhanced internal quantum efficiencies, observed upon Ti(IV) incorporation.

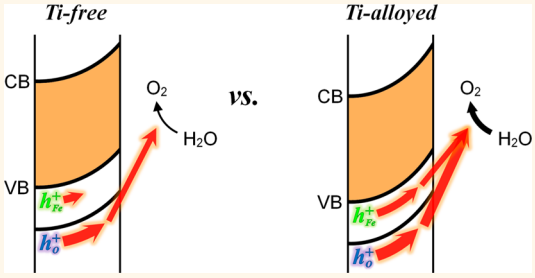

KEYWORDS: iron oxide · titanium incorporation · ultrathin film · absorbed photon-to-current conversion efficiency (APCE) · green light · transient photocurrent

Since the proof-of-concept report by Fujishima and Honda in 1972,[1] photoelectrochemical water splitting has received considerable attention as a potentially promising route for the efficient conversion of solar energy into storable chemical energy. Substantial efforts have been directed toward developing photoelectrodes featuring high chemical stability, low materials cost, and the ability to absorb light over a broad swath of the visible spectrum. Among the many metal oxides examined as photoelectrodes, hematite (α-Fe_2O_3) is one of the most effective materials at meeting these particular requirements.[2−4] Extended spectral coverage is achieved by exploiting two general types of transitions.[5,6] The first covers the UV and blue part of the spectrum and corresponds to an allowed (direct) excitation possessing substantial O(2p) → Fe(3d) character (see Supporting Information for additional explanations).[7] The second is a forbidden (indirect) excitation having substantial Fe(3d) → Fe(3d) character. This transition enables hematite to absorb green photons.[5]

However, there exist significant challenges, including (a) low absorption cross sections in the visible and, especially, midvisible region, (b) slow kinetics for oxygen evolution, and (c) low internal quantum efficiencies for O_2 production, especially by holes photogenerated by Fe(3d) → Fe(3d) excitation (*i.e.*, absorption of green light).[8−10] Challenge b results in low photovoltages, while challenges a and c are manifest as low photocurrents. Indeed, the best hematite-based photoelectrodes typically yield only about a quarter to a third of the photocurrent density expected for an optimally performing electrode absorbing to ca. 610 nm (*i.e.*, ~3.5 to 4.3 mA cm^{-2} *vs* ~13 mA cm^{-2}).[11−14] Low internal quantum efficiencies (or absorbed photon-to-current conversion efficiencies, APCEs) are consequences of both slow oxygen evolution reaction (OER) kinetics relative to rates of surface-mediated electron/hole recombination and inefficient delivery of photogenerated holes

* Address correspondence to j-hupp@northwestern.edu.

Received for review July 15, 2014 and accepted November 21, 2014.

Published online November 21, 2014
10.1021/nn503869n

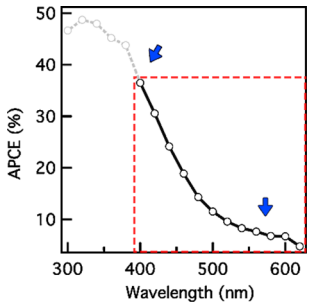

Figure 1. Absorbed photon-to-current conversion efficiency of planar hematite film (25 nm). Adapted from ref 15. Copyright 2011 American Chemical Society.

to the electrode/solution interface (due to recombination of electrons and holes within the photoelectrode). Effective internal recombination, in turn, reflects the short lifetimes (a few to several picoseconds) and the resulting short transport distances for photogenerated holes (a few to several nanometers in bulk, polycrystalline hematite), especially relative to required optical path lengths (*e.g.*, 120 and 2500 nm for 90% light absorption at 450 and 600 nm, respectively).

Figure 1, from the work by Lin and co-workers,[15] provides striking illustrations of both the low *internal* quantum efficiencies (APCE values) for photoelectrochemical production of dioxygen and the strong dependence of these yields on excitation wavelength. Note that the data in the figure were obtained with an exceptionally thin photoelectrode (ca. 25 nm thickness) in order to ameliorate, at least partially, problems associated with short hole-transport distances. Note also that over the region where α-Fe_2O_3 absorbs, APCE values vary from ca. 50% at 300 nm to less than 5% at 600 nm. The greater than 10-fold difference for UV *versus* green illumination could conceivably reflect (a) differences in interfacial chemical reactivity for holes generated in the oxygen-dominated portion of the valence band (h^+_O) versus the iron-dominated portion (h^+_{Fe}), (b) shorter lifetimes for iron-sited *versus* oxygen-sited holes, (c) slower transport for iron-sited *versus* oxygen-sited holes, (d) sizable differences in depth of light penetration, resulting in creation of h^+_{Fe} at distances much further (on average) from the electrode/solution interface than those for h^+_O, and/or (e) other effects. Explanation c is qualitatively compatible with a much greater degree of localization of h^+_{Fe} than h^+_O. Explanation d, while likely significant in some circumstances, is comparatively unimportant for thin, optically dilute photoelectrodes. Regardless, the observed low APCE values for hematite-based photoanodes, especially at longer wavelengths, translate directly into much smaller than ideal values for overall photocurrent density.

Previous efforts to address these challenges have largely focused on (a) design of photoanodes possessing favorably nanostructured architectures,[13,16−18] (b) orthogonalization of light-collection and hole-delivery directions and dimensions (for example, by constructing ultrathin coatings of α-Fe_2O_3 on high-surface-area, conductive scaffolds[15,19−21]), (c) plasmonic[22−24] or other enhancement of light collection (thereby permitting thinner electrodes to be employed), (d) photoelectrode surface modification to accelerate OER kinetics[11,25−27] and/or inhibit surface-mediated charge recombination, (e) improvement of hematite/current-collector epitaxy (for example, by treatment of conductive glass with silicon[28] or gallium ions[29]), so as to diminish interfacial dead-layer behavior,[30] and/or (f) alloying of modest amounts of different elements, such as ions of Sn,[31,32] Ti,[30,33−40] Ni,[41] Si,[16,42,43] Co,[17] and Al,[44] to engender any of several positive attributes.

Among these efforts, bulk incorporation of secondary metals has been at least moderately successful. On the basis of previous studies, it appears that substituted elements can act as electron donors and thus increase the carrier density,[31−36,38−41] can act as OER catalysts,[41] can act as passivators of surface states and grain boundaries responsible for electron/hole recombination,[33,42] and can favorably affect crystallinity.[37,44] Glasscock *et al.*[33] reported that alloyed Ti(IV) passivates grain boundaries and surface states as well as increases electrical conductivity. Li's group[31,34] also concluded that the incorporation of Sn(IV) and/or Ti(IV) increased the carrier density in hematite, whereas work by Zandi *et al.*[30] showed that the carrier density was not appreciably affected by Ti(IV) incorporation; instead they concluded that incorporated Ti(IV) served mainly to alleviate the dead layer effect, and thereby improve hole delivery to the electrode/solution interface. However, given differences in methods of electrode fabrication and in resulting hematite morphology, the differing conclusions are not necessarily indicative of contradictory findings. In other words, the role of Ti additives in hematite is not yet fully understood. However, it can be agreed that titanium substitution does favorably influence photocatalytic oxidation of water by hematite, most likely *via* multiple mechanisms. Therefore, systematic studies focused on the charge collection properties, with minimization of the complications caused by other factors, is necessary to more efficiently use Ti as an additive of hematite photoelectrodes.

Herein we report the results of Ti(IV) alloying of thin and ultrathin films of hematite synthesized *via* atomic layer deposition (ALD), as they relate to photocatalytic water oxidation. We reasoned that ALD-synthesized flat films, in contrast to various nanostructured architectures, would exhibit minimal light scattering, and thus enable semiconductor absorptance to be readily quantified. We additionally reasoned that thin-film electrodes would be free from complications due to low electrical conductivity. Finally, we reasoned that if alloying engendered changes in carrier concentration and, in turn, band-bending and charge-transport

dynamics, the consequences for photocatalysis would be maximized by assembling films having thicknesses comparable to those of the semiconductor's space-charge layer.

As detailed below, we find that incorporation of modest amounts of Ti(IV) in thin and ultrathin hematite films (1) suppresses surface recombination of photogenerated holes and electrons, (2) enhances the efficiency of delivery of photogenerated holes to the electrode/solution interface, especially holes formed *via* nominal Fe(3d) → Fe(3d) excitation (green excitation), and (3) boosts photovoltages and limiting densities of photocurrents. The green-light enhancing behavior is noticeably amplified as the photoelectrode is made thinner, with the most striking effects being seen with Ti-alloyed, crystalline films of Fe_2O_3 films having depths of just 6 nm. We additionally find that, upon reaching the electrode/solution interface and engaging in water oxidation, holes generated by direct excitation (blue excitation) behave identically to those generated *via* excitation of the Fe(3d) → Fe(3d)-like transition (green excitation).

RESULTS AND DISCUSSION

Photoelectrochemical Performance of Ultrathin Films Fabricated by ALD. Although hematite thin films have been fabricated by various techniques, including sol–gel reaction,[45] electrodeposition,[44,46] spray pyrolysis,[47] chemical vapor deposition,[35,48] and atomic layer deposition,[15,49–52] ALD is uniquely suited for ultrathin film studies. Specifically, its self-limiting nature allows for the atomic level control of thickness and for conformal deposition.[53–56] In a typical hematite film synthesis, ferrocene and ozone were used as precursors, whereas Ti-substituted hematite thin films were fabricated by systematically exposing substrates to ferrocene/ozone[49] and titanium(IV)isopropoxide (TTIP)/water.

Figure 2 shows a representative cross-sectional transmission electron microscopy (TEM) image of an ultrathin hematite film in which 3.4% of the Fe centers have been substituted by Ti as determined by XRF. The 11 nm film, deposited on an FTO substrate, is highly uniform, smooth, and conformal. Lattice images (for example, Figure 2b) show the film (after annealing) to be highly crystalline, with lattice fringe spacings of 0.27 and 0.25 nm, corresponding, respectively, to the interlayer spacings of the (104) and (110) planes of hematite. Although not shown, similar crystallinity is also evident for both thicker (17 nm) and thinner (6 nm) films. To our knowledge, no other film fabrication approaches have been found to be capable of producing crystalline Fe_2O_3 films as thin as 6 nm.

Figure 3 shows representative photocurrent density–potential (*J*–*V*) curves (three-electrode cells) in aqueous solution at pH 13.6 (*i.e.*, 1 M NaOH). For Ti-free hematite, the water oxidation photocurrent begins at about 1.2 V vs RHE, rises to 0.01 mA cm^{-2} at 1.26 V vs RHE and reaches 0.15 mA cm^{-2} at 1.53 V vs RHE. Ti-substituted hematite films exhibit higher photoelectrochemical performance compared with that of Ti-free hematite. With increasing Ti content, the photoelectrochemical performance is gradually improved, with the highest performance being achieved with 3.4% Ti. (extension to 8.0% Ti results in some loss of performance; see figure.) Close inspection of the photoelectrochemical plots shows that Ti-alloying improves values of both photovoltages and limiting photocurrents.

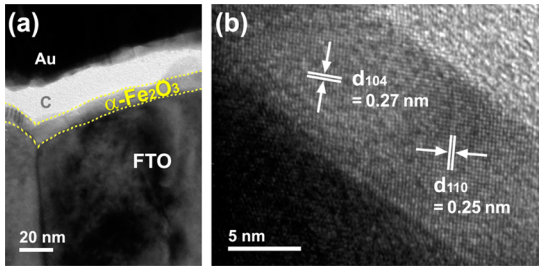

Figure 2. (a) Cross-sectional TEM image and (b) high resolution TEM image of 3.4% Ti-substituted hematite thin film deposited on FTO by ALD.

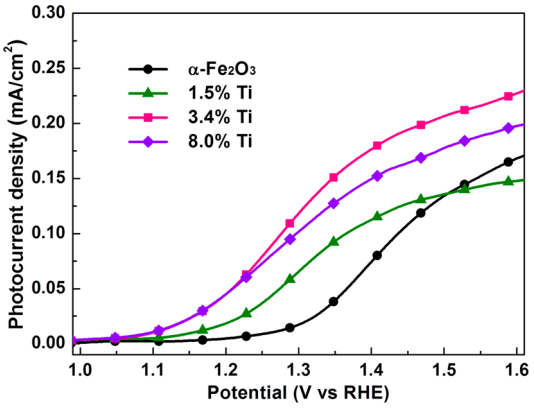

Figure 3. Photocurrent density–potential curves of Ti-free and Ti(IV)-alloyed hematite films with thickness of 11 nm.

Structural and Electronic Properties. Given findings for other metal oxides (albeit, with rather different additives), Ti(IV) incorporation could conceivably alter the absorptance and/or the band gap of α-Fe_2O_3. For example, the photoelectrochemical performance of WO_3 as a water oxidation catalyst has been reported to improve significantly by incorporating N_2 within the oxide lattice. The improvement is due largely to a decrease in the band gap for direct excitation and, therefore, to improved light harvesting. The band gap modulation, in turn, has been ascribed mainly to lattice distortions, although recruitment and mixing of filled nitrogen orbitals with the valence band of tungsten trioxide.[57] As noted above, flat, ALD-fabricated films on transparent platforms such as conductive glass lend themselves to quantitative assessment of absorption properties, as complications from light scattering are largely absent. Figure 4 shows that, within experimental uncertainty,

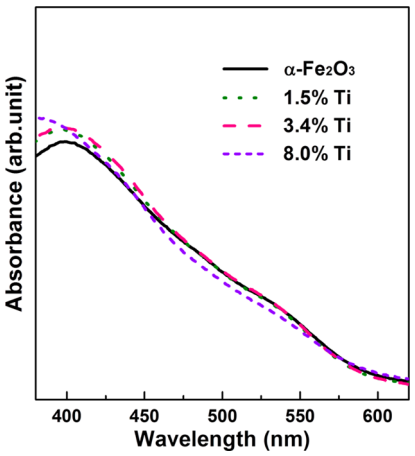

Figure 4. Optical absorption spectra of Ti-free and Ti-substituted hematite films with thickness of 11 nm. Measurements have been corrected for residual light-scattering.

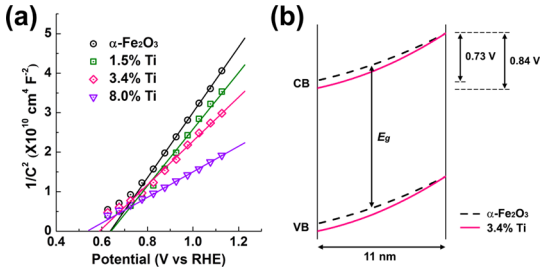

Figure 5. (a) Mott–Schottky plots and (b) schematic band diagram based on the calculated electronic parameters for Ti-free and Ti-alloyed hematite thin films with a thickness of 11 nm.

Ti-free and Ti-substituted films of α-Fe_2O_3 have identical visible-region absorption spectra. Differences in photoelectrochemical performance, therefore, cannot be due to differences in light-harvesting efficiencies.

As revealed by polycrystalline thin-film X-ray diffraction (XRD) measurements (Supporting Information, Figure S1), the only crystalline phase present in the annealed, ALD-fabricated samples is hematite. Careful inspection of the patterns shows that the (110) peak shifts to a slightly higher angle as the Ti content increases (inset of Figure S1), implying slight lattice distortion. This observation is consistent with the slight difference in ionic radius for Ti^{4+} (0.605 Å) *versus* that for Fe^{3+} (0.645 Å). Nevertheless, it is difficult to envision how changes in structure that are close to the limit of our ability to detect by thin-film XRD measurements could substantially affect photoelectrochemical behavior.

In principle, substitution of Fe^{3+} by Ti^{4+} should increase the density of charge carriers (*i.e.*, electrons) (N_D). To test this notion, electrochemical impedance measurements were made and Mott–Schottky plots were constructed; see Figure 5a (or Supporting Information, Figure S2). From the inverse slopes of the plots, and as summarized in Table S1, the density of charge carriers indeed does appear to increase with increasing Ti substitution. The increases in carrier density, however, are small, amounting to only about 1% of the values one would expect if each added titanium ion introduced one additional carrier. These results are broadly consistent with those recently reported by Zandi and co-workers.[30]

From the impedance measurements, estimates can also be obtained for the flat band potential (V_{fb}) and the electric potential difference across the space charge layer (ΔV). Additionally, from eq 1 we can obtain estimates for W_{SC}, the width of the space charge layer:

$$W_{SC} = [2\varepsilon_0\varepsilon_s(V - V_{fb})/(qN_D)]^{1/2} \quad (1)$$

In the equation, ε_0 and ε_s are the dielectric constants of free space, semiconductor electrode q is the electronic charge, and V is the applied potential. At 1.53 V vs RHE, as the Ti content increases from 0 to 8%, the values of W_{SC} returned by the equation decrease systematically from 19 to 13 nm, that is, come close to the film thickness (11 nm). Equation 1 is strictly applicable only when the electrode thickness exceeds W_{SC}. Nevertheless, the equation should return useful qualitative information.

These parameters indicate that a higher degree of band bending is achieved near the film surface as a result of Ti alloying, which should lead to a more effective collection of charge carriers. As illustrated in Figure 5b, the increased band bending ($\Delta V_{11nm} = 0.73$ and 0.84 V for Ti-free and 3.4% Ti-substituted hematite, respectively), should elicit a negative shift in the OER onset potential (when J = 0.01 mA cm^{-2}, 1.26 and 1.10 V vs RHE for Ti-free and 3.4% Ti-substituted hematite, respectively), but the observed shift is greater than the increase in band bending. Thus, additional factors, considered in what follows, are likely contributing to the shifts in OER onset potential.

Internal Quantum Efficiencies. To more specifically address the collection yield of photogenerated charge carriers, quantum efficiencies were measured as a function of wavelength. Absorbed photon-to-current conversion efficiencies were obtained by dividing incident photon-to-current conversion efficiencies (IPCEs) (Supporting Information, Figure S3) by light harvesting efficiencies (LHEs) (Figure S4). Figure 6 shows APCE plots for Ti-free and 3.4% Ti-substituted hematite thin films of various thicknesses. In comparison to Ti-free hematite, 3.4% Ti-substituted hematite exhibits enhanced APCEs over the entire wavelength range, and especially in the green wavelength range of 500 to 600 nm. These enhancements are particularly striking for the thinnest films examined (this is also made clear with APCEs of 45 nm films; see Supporting Information, Figure S5), in part because of attenuation of photocurrents ("dead layer" behavior) for the Ti-free material; see panels e and f.

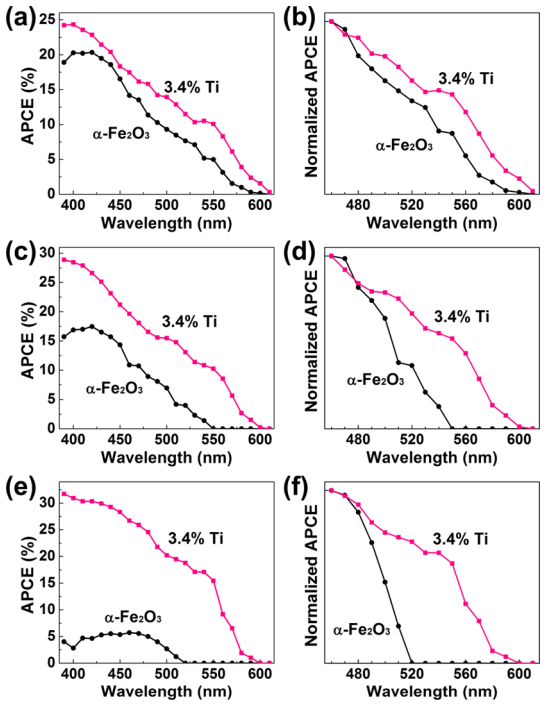

Figure 6. APCE plots measured at a potential of 1.53 V *vs* RHE for Ti-free and Ti-alloyed hematite films with a thickness of (a, b) 17, (c, d) 11, and (e, f) 6 nm.

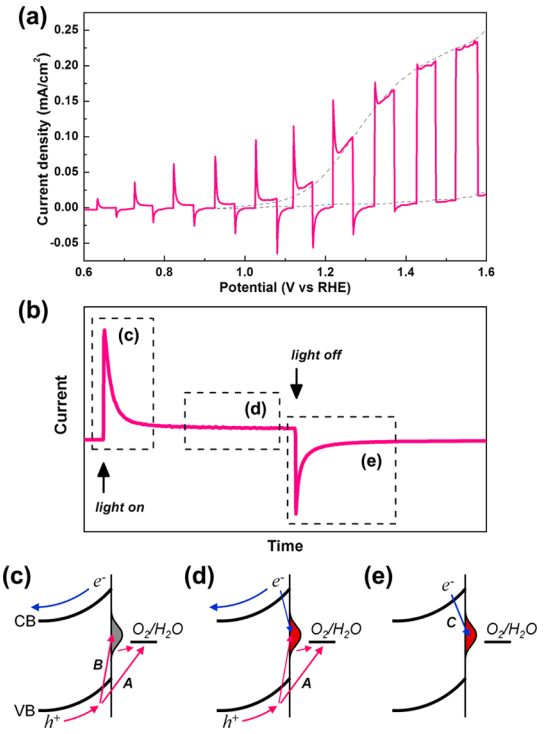

Figure 7. (a) Representative *J*–*V* plot under chopped (white light) illumination. The sample is a 3.4% Ti-substituted hematite film of thickness 11 nm in contact with an aq 1 M NaOH. (b) Expanded view of a representative anodic/cathodic pair of current transients. (c–e) A brief summary of charge-transport processes: (c) when the light is turned on, photogenerated holes move to the electrode surface, and fill surface states and/or react with water. (d) Subsequently, steady-state photocurrent production is obtained. (e) When irradiation is stopped, electrons begin recombining with holes stored in surface states.

Transport and Recombination of Charge Carriers. In an effort to understand how Ti alloying influences the respective internal quantum yields for delivery of h^+_O and h^+_{Fe} to the electrode/solution interface, transient photocurrent measurements were performed under chopped illumination. In most cases, and consistent with earlier reports,[8,58] hematite films show anodic/cathodic current spikes (Figure 7) that appear due to its slow oxygen evolution reaction kinetics. Briefly, when the irradiation is initiated, photogenerated holes move to the surface, and then fill surface states (non-Faradaic current) and/or react with water (Faradaic current) (see Figure 7c). Both processes contribute to the photocurrent at the initial stage, but the non-Faradaic current rapidly decays; the remaining steady-state photocurrent is due only to water oxidation. When the light is turned off, electrons recombine with the holes stored in surface states and this produces cathodic current spikes. Thus, the anodic and cathodic current spikes originate from the charging and discharging of surface states by photogenerated holes, and they are closely related to the rate of surface-mediated recombination of charge carriers.

Given the above behavior with white light, we repeated the experiments using chopped, monochromatic illumination. We recorded current transients based on intermittent excitation of Ti-free and 3.4% Ti-substituted hematite films at 400 nm (direct-gap excitation) and at 550 nm (indirect-gap excitation). The electrodes were of identical thickness (11 nm) and signals were recorded at constant applied potential. Signals were recorded over a range of illumination intensities. By focusing on cathodic transients (dark transients), we eliminated steady-state faradaic contributions. As shown in Supporting Information, Figure S6 (see also Figure 7), the observed sharp cathodic current spikes are followed by decays that can be fit well to two decay time constants (denoted by τ_1 (fast) and τ_2 (slow)). In contrast, the transients are poorly fit by other functions such as second-order decays or single-exponential decays, which is consistent with previous reports.[33,59,60] The density of charge stored in the surface states (denoted by Q_{SS}) is obtainable by integrating the cathodic current transients. As one would anticipate, higher illumination intensities yield large values for Q_{SS}. Additionally, for a given photon flux during the "on" phase, the value for Q_{SS} was observed to be greater for irradiation at 400 nm than 550 nm. This finding is consistent with the substantial differences in light harvesting efficiency at 400 nm versus 550 nm and in subsequent hole-transport efficacy.

Figure 8 shows the relation between τ_2 and Q_{SS}. Interestingly, both Ti-free and Ti-substituted hematite samples exhibit an essentially linear relationship between τ_2 and Q_{SS} (or τ_1 and Q_{SS}; see Supporting Information), regardless of the wavelength of incident light. The commonality of decay times implies

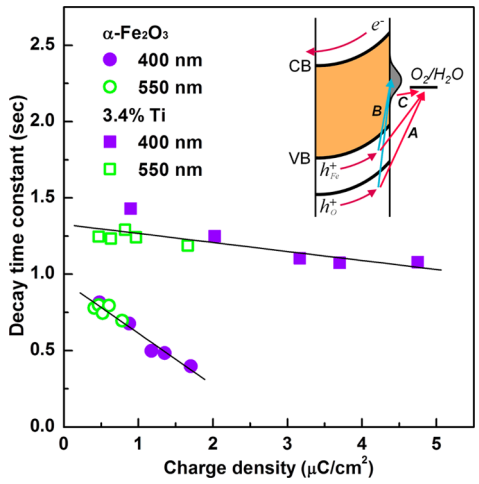

Figure 8. Relation between decay time constants (τ_2) and charge density (Q_{SS}) for Ti-free and 3.4% Ti-substituted hematite thin films. Parameters are obtained from cathodic current transients measured at a potential of 1.23 V *vs* RHE using 400 or 550 nm wavelength light at various intensities. Inset shows charge transport processes that may occur when the electrode is illuminated. Arrows A and C denote water oxidation reactions, while B denotes delivery of holes to surface states.

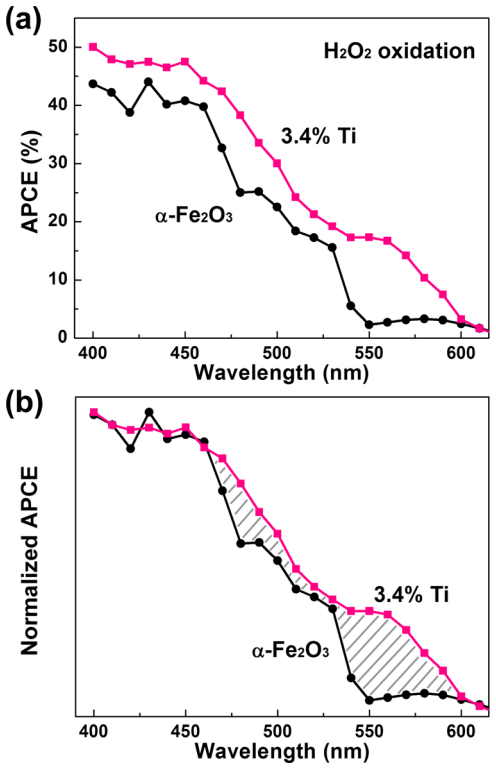

Figure 9. (a) APCE plots for hydrogen peroxide oxidation (*ca.* 1 M) using Ti-free and 3.4% Ti-substituted hematite films with a thickness of 6 nm, which are measured at a potential of 1.0 V *vs* RHE, and (b) their normalized APCE plots.

that, once they reach the surface, holes originating from O 2p have the same reactivity as those of Fe 3d origin. (Note further that the commonality is evident only after accounting for differences in absorptivity at 400 nm versus 550 nm, as well as collection efficiency and other factors, by comparing decay times against measured surface-state charge densities.)

A comparison of the plots in Figure 8 shows that it is clear that under all conditions examined, hole–electron recombination times for Ti-alloyed hematite exceed any observed with Ti-free electrodes. Expressed differently, Ti alloying serves to slow the rates of surface recombination, with the effect becoming more pronounced at higher light intensities. This inhibitory effect is one contributor to the observed enhancement of APCE values for water oxidation by Ti-substituted versus Ti-free hematite. The inhibition of recombination, however, does not account for the markedly greater relative improvement of water oxidation APCE for green light compared to blue light upon Ti incorporation (Figure 6). Clearly effects beyond inhibition of surface-mediated charge recombination must be in play.

We therefore examined the extent to which Ti alloying increases the efficiency of delivery of photogenerated holes to the electrode/solution interface. To do this we measured wavelength-dependent internal quantum efficiency for photo-oxidation of hydrogen peroxide (H_2O_2);[61,62] this substance is sufficiently reactive that essentially every hole that reaches the electrode/solution interface should be captured. The observed absorption-corrected current efficiency, then, should be a measure only of the efficiency of for delivering holes. Quantum efficiencies for H_2O_2 oxidation were measured at a constant potential of 1.0 V vs RHE, where the potential was chosen based on *J*–*V* curves for H_2O_2 oxidation (Supporting Information, Figure S9) to exclude contributions from dark electrolysis. The materials examined were 6 nm thick films of Ti-free and 3.4% Ti-alloyed hematite films.

Figure 9 shows the obtained APCE data. Titanium alloying clearly enhances the efficiency of hole delivery—either by slowing bulk electron–hole recombination or by accelerating hole transport, or both. Over the wavelength range 400 to 530 nm APCE values vary only slightly compared with that at 550 nm. One possible explanation is that recombination occurs *via* the intermediacy of the d–d state, that is, *via* conversion of h^+_O to h^+_{Fe}, with the conversion occurring more readily at longer wavelengths. Returning to Figure 9, the relative efficiency of interface delivery of holes generated over the 400 to 530 nm spectral range is enhanced by Ti alloying by between ~5 and ~30% at most. However, at 550 nm, where the hole is formed *via* Fe(3d) → Fe(3d) excitation, the relative enhancement is a remarkable 1200%. This significant enhancement can also be seen in APCEs measured at different potentials (see Supporting Information). Returning to water oxidation (Figure 7) it is clear the titanium-engendered switching on of photoactivity of thin-film hematite under green illumination (*i.e.*, d–d excitation) is due primarily to attenuation of the yield for bulk recombination of holes and electrons.

As suggested above, an attractive explanation for enhanced efficiency for delivery of photogenerated holes to the electrode surface in ultrathin films is that band-bending engendered by Ti(IV) accelerates the rate of hole transport, where the acceleration is due to increased contributions from migration. We cannot dismiss, however, other potential explanations such as diminution of the rate of electron/hole recombination within the semiconductor (by mechanisms yet to be determined). Regardless, the photochemical consequence is enhancement of APCE values for water oxidation in the range of 500−600 nm, reflecting more effective utilization of h^+_{Fe}. It remains to be seen whether these observations can be exploited in a more significant way so as to yield high-quantum-efficiency, iron oxide-based solar cells for water splitting.

CONCLUSION

Ti(IV) substitution for Fe(III) in ultrathin (*ca.* 6 nm) hematite films is effective for boosting the efficiency of delivery of photogenerated holes to electrode/solution interfaces, especially those holes generated with green photons. While the absorptivity remains essentially unchanged, the increase in hole-collection efficiency, that is, enhanced transport efficiency in the bulk region and reduced surface state recombination rate, results in improved internal quantum efficiencies for water oxidation. Importantly, once delivered to the electrode/solution interface holes generated by allowed O(2p) → Fe(3d)-like excitation at 400 nm display identical chemical reactivity as those generated by partially forbidden Fe(3d) → Fe(3d)-like excitation at 550 nm.

METHODS

Photoelectrode Preparation. Ti-free and Ti-substituted hematite films were deposited on fluorine-doped tin oxide (FTO) by ALD (Savannah 100, Cambridge Nanotech, Inc.). Ferrocene ($Fe(Cp)_2$, 98%, Aldrich) and titanium(IV) isopropoxide (TTIP, 97%, Aldrich) were used as precursors. In a typical deposition of hematite films, $Fe(Cp)_2$ and ozone were used as precursors, whereas Ti(IV)-substituted hematite films were fabricated by alternating depositions of $Fe(Cp)_2$/ozone and TTIP/water. More specifically, $Fe(Cp)_2$ and TTIP were heated to 87 and 80 °C, respectively, whereas substrates were heated to 200 °C. The deposition of hematite was performed according to the following sequence: two 30 s $Fe(Cp)_2$ exposures separated by a 5 s purge and a 30 s purge, then a 30 s ozone exposure. For Ti incorporation, the deposition sequence was as follows: a 1.1 s TTIP exposure and a 15 s purge, followed by a 1.1 s water exposure and a 20 s purge. On the basis of this deposition sequence, the Ti concentration was adjusted by controlling the pulse ratio of Fe/Ti precursors. All films were subsequently annealed at 500 °C for 30 min in air.

Physical Characterization. The crystal structures of the fabricated films were examined by grazing incidence X-ray diffraction (GIXRD, ATX-G, Rigaku). The cross section film was prepared using a focused ion beam (FIB, SMI3050SE, SII Nanotechnology), and its thickness and microstructure were investigated by transmission electron microscopy (TEM, JEM-3000F, JEOL). The optical absorption property was obtained using UV−vis spectroscopy (Cary 5000, Varian), and the elemental composition was measured using X-ray fluorescence (XRF, ED2000, Oxford Instruments).

Electrochemical and Photoelectrochemical Characterization. All electrochemical and photoelectrochemical measurements were performed in 1 M NaOH aqueous solution with a platinum counter electrode and Ag/AgCl (saturated KCl) reference electrode. The photocurrent densities and incident photon-to-current conversion efficiencies (IPCEs) were evaluated using a potentiostat (CHI 1202, CH Instruments). The light source was a xenon lamp equipped with an AM 1.5 filter, and the power of filtered light was calibrated by an optical power meter and a silicon photodiode (PV Measurements, Inc.). Electrochemical impedance spectroscopy was performed using a Solartron Analytical Modulab electrochemical analyzer with a 10 mV AC perturbation under biases ranging between 0.6 and 1.2 V *vs* RHE.

Conflict of Interest: The authors declare no competing financial interest.

Supporting Information Available: Results of XRD, Mott−Schottky plots, quantum efficiency spectra, LHE spectra, *J*−*V* curves, transient current plots, and decay time plot. This material is available free of charge *via* the Internet at http://pubs.acs.org.

Acknowledgment. We thank Dr. Benjamin Klahr for helpful discussions and critical reading of the manuscript. This work was supported as part of the ANSER Center, an Energy Frontier Research Center funded by the U.S. Department of Energy, Office of Science, Office of Basic Energy Sciences under Award Number DE-SC0001059.

REFERENCES AND NOTES

1. Fujishima, A.; Honda, K. Electrochemical Photolysis of Water at a Semiconductor Electrode. *Nature* **1972**, *238*, 37–38.
2. Hardee, K. L.; Bard, A. J. Semiconductor Electrodes: V. The Application of Chemically Vapor Deposited Iron Oxide Films to Photosensitized Electrolysis. *J. Electrochem. Soc.* **1976**, *123*, 1024–1026.
3. Sivula, K.; Formal, F. L.; Grätzel, M. Solar Water Splitting: Progress Using Hematite (α-Fe_2O_3) Photoelectrodes. *ChemSusChem* **2011**, *4*, 432–449.
4. Katz, M. J.; Riha, S. C.; Jeong, N. C.; Martinson, A. B. F.; Farha, O. K.; Hupp, J. T. Toward Solar Fuels: Water Splitting with Sunlight and "Rust"? *Coord. Chem. Rev.* **2012**, *256*, 2521–2529.
5. Marusak, L. A.; Messier, R.; White, W. B. Optical Absorption Spectrum of Hematite, α-Fe_2O_3 near IR to UV. *J. Phys. Chem. Solids* **1980**, *41*, 981–984.
6. Thimsen, E.; Biswas, S.; Lo, C. S.; Biswas, P. Predicting the Band Structure of Mixed Transition Metal Oxides: Theory and Experiment. *J. Phys. Chem. C* **2009**, *113*, 2014–2021.
7. Vura-Weis, J.; Jiang, C.-M.; Liu, C.; Gao, H.; Lucas, J. M.; Groot, F. M. F.; Yang, P.; Alivisatos, A. P.; Leone, S. R. Femtosecond $M_{2,3}$-Edge Spectroscopy of Transition-Metal Oxides: Photoinduced Oxidation State Change in α-Fe_2O_3. *J. Phys. Chem. Lett.* **2013**, *4*, 3667–3671.
8. Dare-Edwards, M. P.; Goodenough, J. B.; Hamnett, A.; Trevellick, P. R. Electrochemistry and Photoelectrochemistry of Iron(III) Oxide. *J. Chem. Soc., Faraday Trans.* **1983**, *79*, 2027–2041.
9. Kennedy, J. H.; Frese, K. W. Photooxidation of Water at α-Fe_2O_3 Electrodes. *J. Electrochem. Soc.* **1978**, *125*, 709–714.
10. Braun, A.; Sivula, K.; Bora, D. K.; Zhu, J.; Zhang, L.; Grätzel, M.; Guo, J.; Constable, E. C. Direct Observation of Two Electron Holes in a Hematite Photoanode during Photoelectrochemical Water Splitting. *J. Phys. Chem. C* **2012**, *116*, 16870–16875.

11. Tilley, S. D.; Cornuz, M.; Sivula, K.; Grätzel, M. Light-Induced Water Splitting with Hematite: Improved Nanostructure and Iridium Oxide Catalysis. *Angew. Chem., Int. Ed.* **2010**, *49*, 6405–6408.
12. Chen, Z.; Jaramillo, T. F.; Deutsch, T. G.; Kleiman-Shwarsctein, A.; Forman, A. J.; Gaillard, N.; Garland, R.; Takanabe, K.; Heske, C.; Sunkara, M.; *et al*. Accelerating Materials Development for Photoelectrochemical Hydrogen Production: Standards for Methods, Definitions, and Reporting Protocols. *J. Mater. Res.* **2010**, *25*, 3–16.
13. Warren, S. C.; Voïtchovsky, K.; Dotan, H.; Leroy, C. M.; Cornuz, M.; Stellacci, F.; Hébert, C.; Rothschild, A.; Grätzel, M. Identifying Champion Nanostructures for Solar Water-Splitting. *Nat. Mater.* **2013**, *12*, 842–849.
14. Kim, J. Y.; Magesh, G.; Youn, D. H.; Jang, J.-W.; Kubota, J.; Domen, K.; Lee, J. S. Single-Crystalline, Wormlike Hematite Photoanodes for Efficient Solar Water Splitting. *Sci. Rep.* **2014**, *3*, 2681.
15. Lin, Y.; Zhou, S.; Sheehan, S. W.; Wang, D. Nanonet-Based Hematite Heteronanostructures for Efficient Solar Water Splitting. *J. Am. Chem. Soc.* **2011**, *133*, 2398–2401.
16. Kay, A.; Cesar, I.; Grätzel, M. New Benchmark for Water Photooxidation by Nanostructured α-Fe_2O_3 Films. *J. Am. Chem. Soc.* **2006**, *128*, 15714–15721.
17. Hou, Y.; Zuo, F.; Dagg, A.; Feng, P. A Three-Dimensional Branched Cobalt-Doped α-Fe_2O_3 Nanorod/$MgFe_2O_4$ Heterojunction Array as a Flexible Photoanode for Efficient Photoelectrochemical Water Oxidation. *Angew. Chem., Int. Ed.* **2013**, *52*, 1248–1252.
18. LaTempa, T. J.; Feng, X.; Paulose, M.; Grimes, C. A. Temperature-Dependent Growth of Self-Assembled Hematite (α-Fe_2O_3) Nanotube Arrays: Rapid Electrochemical Synthesis and Photoelectrochemical Properties. *J. Phys. Chem. C* **2009**, *113*, 16293–16298.
19. Riha, S. C.; Vermeer, M. J. D.; Pellin, M. J.; Hupp, J. T.; Martinson, A. B. F. Hematite-Based Photo-oxidation of Water Using Transparent Distributed Current Collectors. *ACS Appl. Mater. Interface* **2013**, *5*, 360–367.
20. Stefik, M.; Cornuz, M.; Mathews, N.; Hisatomi, T.; Mhaisalkar, S.; Grätzel, M. Transparent, Conducting Nb:SnO_2 for Host–Guest Photoelectrochemistry. *Nano Lett.* **2012**, *12*, 5431–5435.
21. Qiu, Y.; Leung, S.-F.; Zhang, Q.; Hua, B.; Lin, Q.; Wei, Z.; Tsui, K.-H.; Zhang, Y.; Yang, S.; Fan, Z. Efficient Photoelectrochemical Water Splitting with Ultrathin Films of Hematite on Three-Dimensional Nanophotonic Structures. *Nano Lett.* **2014**, *14*, 2123–2129.
22. Thimsen, E.; Formal, F. L.; Grätzel, M.; Warren, S. C. Influence of Plasmonic Au Nanoparticles on the Photoactivity of Fe_2O_3 Electrodes for Water Splitting. *Nano Lett.* **2011**, *11*, 35–43.
23. Warren, S. C.; Thimsen, E. Plasmonic Solar Water Splitting. *Energy Environ. Sci.* **2012**, *5*, 5133–5146.
24. Thomann, I.; Pinaud, B. A.; Chen, Z.; Clemens, B. M.; Jaramillo, T. F.; Brongersma, M. L. Plasmon Enhanced Solar-to-Fuel Energy Conversion. *Nano Lett.* **2011**, *11*, 3440–3446.
25. Barroso, M.; Cowan, A. J.; Pendlebury, S. R.; Grätzel, M.; Klug, D. R.; Durrant, J. R. The Role of Cobalt Phosphate in Enhancing the Photocatalytic Activity of α-Fe_2O_3 toward Water Oxidation. *J. Am. Chem. Soc.* **2011**, *133*, 14868–14871.
26. Zhong, D. K.; Sun, J.; Inumaru, H.; Gamelin, D. R. Solar Water Oxidation by Composite Catalyst/α-Fe_2O_3 Photoanodes. *J. Am. Chem. Soc.* **2009**, *131*, 6086–6087.
27. Riha, S. C.; Klahr, B. M.; Tyo, E. C.; Seifert, S.; Vajda, S.; Pellin, M. J.; Hamann, T. W.; Martinson, A. B. F. Atomic Layer Deposition of a Submonolayer Catalyst for the Enhanced Photoelectrochemical Performance of Water Oxidation with Hematite. *ACS Nano* **2013**, *7*, 2396–2405.
28. Formal, F. L.; Grätzel, M.; Sivula, K. Controlling Photoactivity in Ultrathin Hematite Films for Solar Water-Splitting. *Adv. Funct. Mater.* **2010**, *20*, 1099–1107.
29. Hisatomi, T.; Brillet, J.; Cornuz, M.; Formal, F. L.; Tétreault, N.; Sivula, K.; Grätzel, M. A Ga_2O_3 Underlayer as an Isomorphic Template for Ultrathin Hematite Films toward Efficient Photoelectrochemical Water Splitting. *Faraday Discuss.* **2012**, *155*, 223–232.
30. Zandi, O.; Klahr, B. M.; Hamann, T. W. Highly Photoactive Ti-Doped α-Fe_2O_3 Thin Film Electrodes: Resurrection of the Dead Layer. *Energy Environ. Sci.* **2013**, *6*, 634–642.
31. Ling, Y.; Wang, G.; Wheeler, D. A.; Zhang, J. Z.; Li, Y. Sn-Doped Hematite Nanostructures for Photoelectrochemical Water Splitting. *Nano Lett.* **2011**, *11*, 2119–2125.
32. Bohn, C. D.; Agrawal, A. K.; Walter, E. C.; Vaudin, M. D.; Herzing, A. A.; Haney, P. M.; Talin, A. A.; Szalai, V. A. Effect of Tin Doping on α-Fe_2O_3 Photoanodes for Water Splitting. *J. Phys. Chem. C* **2012**, *116*, 15290–15296.
33. Glasscock, J. A.; Barnes, P. R. F.; Plumb, I. C.; Savvides, N. Enhancement of Photoelectrochemical Hydrogen Production from Hematite Thin Films by the Introduction of Ti and Si. *J. Phys. Chem. C* **2007**, *111*, 16477–16488.
34. Wang, G.; Ling, Y.; Wheeler, D. A.; George, K. E. N.; Horsley, K.; Heske, C.; Zhang, J. Z.; Li, Y. Facile Synthesis of Highly Photoactive α-Fe_2O_3-Based Films for Water Oxidation. *Nano Lett.* **2011**, *11*, 3503–3509.
35. Hahn, N. T.; Mullins, C. B. Photoelectrochemical Performance of Nanostructured Ti- and Sn-Doped α-Fe_2O_3 Photoanodes. *Chem. Mater.* **2010**, *22*, 6474–6482.
36. Miao, C.; Shi, T.; Xu, G.; Ji, S.; Ye, C. Photocurrent Enhancement for Ti-Doped Fe_2O_3 Thin Film Photoanodes by an *In Situ* Solid-State Reaction Method. *ACS Appl. Mater. Interface* **2013**, *5*, 1310–1316.
37. Zhang, P.; Kleiman-Shwarsctein, A.; Hu, Y.-S.; Lefton, J.; Sharma, S.; Forman, A. J.; McFarland, E. Oriented Ti Doped Hematite Thin Film as Active Photoanodes Synthesized by Facile APCVD. *Energy Environ. Sci.* **2011**, *4*, 1020–1028.
38. Rioult, M.; Magnan, H.; Stanescu, D.; Barbier, A. Single Crystalline Hematite Films for Solar Water Splitting: Ti-Doping and Thickness Effects. *J. Phys. Chem. C* **2014**, *118*, 3007–3014.
39. Tang, H.; Matin, M. A.; Wang, H.; Deutsch, T.; Al-Jassim, M.; Turner, J.; Yan, Y. Synthesis and Characterization of Titanium-Alloyed Hematite Thin Films for Photoelectrochemical Water Splitting. *J. Appl. Phys.* **2011**, *110*, 123511.
40. Zhang, M.; Luo, W.; Li, Z.; Yu, T.; Zou, Z. Improved Photoelectrochemical Responses of Si and Ti Codoped α-Fe_2O_3 Photoanode Films. *Appl. Phys. Lett.* **2010**, *97*, 042105.
41. Cheng, W.; He, J.; Sun, Z.; Peng, Y.; Yao, T.; Liu, Q.; Jiang, Y.; Hu, F.; Xie, Z.; He, B.; *et al*. Ni-Doped Overlayer Hematite Nanotube: A Highly Photoactive Architecture for Utilization of Visible Light. *J. Phys. Chem. C* **2012**, *116*, 24060–24067.
42. Chemelewski, W. D.; Hahn, N. T.; Mullins, C. B. Effect of Si Doping and Porosity on Hematite's (α-Fe_2O_3) Photoelectrochemical Water Oxidation Performance. *J. Phys. Chem. C* **2012**, *116*, 5255–5261.
43. Saremi-Yarahmadi, S.; Wijayantha, K. G. U.; Tahir, A. A.; Vaidhyanathan, B. Nanostructured α-Fe_2O_3 Electrodes for Solar Driven Water Splitting: Effect of Doping Agents on Preparation and Performance. *J. Phys. Chem. C* **2009**, *113*, 4768–4778.
44. Kleiman-Shwarsctein, A.; Huda, M. N.; Walsh, A.; Yan, Y.; Stucky, G. D.; Hu, Y.-S.; Al-Jassim, M. M.; McFarland, E. W. Electrodeposited Aluminum-Doped α-Fe_2O_3 Photoelectrodes: Experiment and Theory. *Chem. Mater.* **2010**, *22*, 510–517.
45. Hamd, W.; Cobo, S.; Fize, J.; Baldinozzi, G.; Schwartz, W.; Reymermier, M.; Pereira, A.; Fontecave, M.; Artero, V.; Laberty-Robert, C.; *et al*. Mesoporous α-Fe_2O_3 Thin Films Synthesized *via* the Sol-Gel Process for Light-Driven Water Oxidation. *Phys. Chem. Chem. Phys.* **2012**, *14*, 13224–13232.
46. Liu, Y.; Yu, Y.-X.; Zhang, W.-D. Photoelectrochemical Properties of Ni-Doped Fe_2O_3 Thin Films Prepared by Electrodeposition. *Electrochim. Acta* **2012**, *59*, 121–127.
47. Duret, A.; Grätzel, M. Visible Light-Induced Water Oxidation on Mesoscopic α-Fe_2O_3 Films Made by Ultrasonic Spray Pyrolysis. *J. Phys. Chem. B* **2005**, *109*, 17184–17191.
48. Zhong, D. K.; Gamelin, D. R. Photoelectrochemical Water Oxidation by Cobalt Catalyst ("Co-Pi")/α-Fe_2O_3 Composite

Photoanodes: Oxygen Evolution and Resolution of a Kinetic Bottleneck. *J. Am. Chem. Soc.* **2010**, *132*, 4202–4207.
49. Martinson, A. B. F.; DeVries, M. J.; Libera, J. A.; Christensen, S. T.; Hupp, J. T.; Pellin, M. J.; Elam, J. W. Atomic Layer Deposition of Fe_2O_3 Using Ferrocene and Ozone. *J. Phys. Chem. C* **2011**, *115*, 4333–4339.
50. Klug, J. A.; Becker, N. G.; Riha, S. C.; Martinson, A. B. F.; Elam, J. W.; Pellin, M. J.; Proslier, T. Low Temperature Atomic Layer Deposition of Highly Photoactive Hematite Using Iron(III) Chloride and Water. *J. Mater. Chem. A* **2013**, *1*, 11607–11613.
51. Riha, S. C.; Racowski, J. M.; Lanci, M. P.; Klug, J. A.; Hock, A. S.; Martinson, A. B. F. Phase Discrimination through Oxidant Selection in Low-Temperature Atomic Layer Deposition of Crystalline Iron Oxides. *Langmuir* **2013**, *29*, 3439–3445.
52. Ridder, M.; Ven, P. C.; Welzenis, R. G.; Brongersma, H. H.; Helfensteyn, S.; Creemers, C.; Voort, P. V. D.; Baltes, M.; Mathieu, M.; Vansant, E. F. Growth of Iron Oxide on Yttria-Stabilized Zirconia by Atomic Layer Deposition. *J. Phys. Chem. B* **2002**, *106*, 13146–13153.
53. Suntola, T. Atomic Layer Epitaxy. *Mater. Sci. Rep.* **1989**, *4*, 261–312.
54. Ritala, M.; Leskelä, M.; Dekker, J.-P.; Mutsaers, C.; Soininen, P. J.; Skarp, J. Perfectly Conformal TiN and Al_2O_3 Films Deposited by Atomic Layer Deposition. *Chem. Vap. Dep.* **1999**, *5*, 7–9.
55. Leskelä, M.; Ritala, M. Atomic Layer Deposition Chemistry: Recent Developments and Future Challenges. *Angew. Chem., Int. Ed.* **2003**, *42*, 5548–5554.
56. George, S. M. Atomic Layer Deposition: An Overview. *Chem. Rev.* **2010**, *110*, 111–131.
57. Mi, Q.; Ping, Y.; Li, Y.; Cao, B.; Brunschwig, B. S.; Khalifah, P. G.; Galli, G. A.; Gray, H. B.; Lewis, N. S. Thermally Stable N_2-Intercalated WO_3 Photoanodes for Water Oxidation. *J. Am. Chem. Soc.* **2012**, *134*, 18318–18324.
58. Hardee, K. L.; Bard, A. J. Semiconductor Electrodes: X. Photoelectrochemical Behavior of Several Polycrystalline Metal Oxide Electrodes in Aqueous Solutions. *J. Electrochem. Soc.* **1977**, *124*, 215–224.
59. Klahr, B.; Gimenez, S.; Fabregat-Santiago, F.; Bisquert, J.; Hamann, T. W. Electrochemical and Photoelectrochemical Investigation of Water Oxidation with Hematite Electrodes. *Energy Environ. Sci.* **2012**, *5*, 7626–7636.
60. Formal, F. L.; Sivula, K.; Grätzel, M. The Transient Photocurrent and Photovoltage Behavior of a Hematite Photoanode under Working Conditions and the Influence of Surface Treatments. *J. Phys. Chem. C* **2012**, *116*, 26707–26720.
61. Itoh, K.; Bockris, J. O. M. Thin Film Photoelectrochemistry: Iron Oxide. *J. Electrochem. Soc.* **1984**, *131*, 1266–1271.
62. Dotan, H.; Sivula, K.; Grätzel, M.; Rothschild, A.; Warren, S. C. Probing the Photoelectrochemical Properties of Hematite (α-Fe_2O_3) Electrodes using Hydrogen Peroxide as a Hole Scavenger. *Energy Environ. Sci.* **2011**, *4*, 958–964.